Persistence of Charge Ordering Instability to Coulomb Engineering in the Excitonic Insulator Candidate $TiSe_2$

Sebastian Buchberger,[1,2] Yann in 't Veld,[3] Akhil Rajan,[1] Philip A. E. Murgatroyd,[1] Brendan Edwards,[1] Bruno K. Saika,[1] Naina Kushwaha,[1,4] Maria H. Visscher,[1,2] Jan Berges,[5] Dina Carbone,[6] Jacek Osiecki,[6] Craig Polley,[6] Tim Wehling,[3,7,*] and Phil D. C. King[1,†]

[1]*SUPA, School of Physics and Astronomy, University of St Andrews, St Andrews KY16 9SS, United Kingdom*
[2]*Max Planck Institute for Chemical Physics of Solids, Nöthnitzer Strasse 40, D-01187 Dresden, Germany*
[3]*I. Institute of Theoretical Physics, Universität Hamburg, D-22607 Hamburg, Germany*
[4]*STFC Central Laser Facility, Research Complex at Harwell, Harwell Campus, Didcot OX11 0QX, United Kingdom*
[5]*Bremen Center for Computational Materials Science, and MAPEX Center for Materials and Processes, University of Bremen, D-28359 Bremen, Germany*
[6]*MAX IV Laboratory, Lund University, Lund, Sweden*
[7]*The Hamburg Centre for Ultrafast Imaging, D-22761 Hamburg, Germany*

(Received 30 May 2025; revised 29 August 2025; accepted 9 October 2025; published 12 November 2025)

$TiSe_2$ has long been considered one of the best candidate materials to host the elusive excitonic insulator (EI) phase. However, a finite coupling to the lattice can generically be expected, while a lack of "smoking-gun" signatures for the importance of the electron-hole interaction in driving the phase transition has rendered it challenging to distinguish the EI from the conventional charge-density wave (CDW) phase. Here, we demonstrate a new approach, exploiting the susceptibility of excitons to dielectric screening. We combine mechanical exfoliation with molecular-beam epitaxy to fabricate ultraclean van der Waals heterostructures of monolayer (ML) $TiSe_2$/graphite and ML $TiSe_2/h$-BN. We observe how the modified substrate screening environment drives a renormalization of the quasiparticle band gap of the $TiSe_2$ layer, signifying its susceptibility to Coulomb engineering. The temperature-dependent evolution of its electronic structure, however, remains unaffected, indicating that excitons are not required to drive the CDW transition in $TiSe_2$.

DOI: 10.1103/9trc-9865 Subject Areas: Condensed Matter Physics

I. INTRODUCTION

For the past half century, $TiSe_2$ has been one of the most actively studied and controversial members of the family of transition metal dichalcogenides. Its normal state electronic structure is best described as an indirect-gap semiconductor with close to zero band gap [Fig. 1(a)] [1–4]. This is, in principle, the ideal band structure to support the formation of an excitonic insulator (EI), an exotic state where electrons and holes spontaneously form excitons and Bose condense, driving a transition into a charge ordered state [5,6]. The observation of a charge-density wave (CDW) instability occurring at around 200 K therefore generated significant excitement, and $TiSe_2$ has been proposed as one of the most likely candidate materials to host the EI phase [1,2,7–9]. However, this mechanism has been questioned in favor of a simple structural phase transition [10–12], where the charge density merely follows the periodic lattice distortion due to electron-phonon coupling. Importantly, both mechanisms break the same underlying symmetries of the crystal, and give rise to essentially identical electronic structures in the ordered state [Fig. 1(b)]; it is therefore extremely challenging from studying either the crystal or electronic structure to establish which of excitonic or lattice contributions plays the dominant role in driving the phase transition. Despite numerous attempts to answer this question—for example, by probing the collective excitations of $TiSe_2$ [13,14] or the response of its ordering instability to ultrafast optical excitation [15–18]—the origin of the phase transition in $TiSe_2$ remains highly controversial.

Here, we employ a different approach: We study monolayers of $TiSe_2$, where we statically modify the dielectric screening by control of the environment. It is well known

*Contact author: tim.wehling@physik.uni-hamburg.de
†Contact author: pdk6@st-andrews.ac.uk

Published by the American Physical Society under the terms of the Creative Commons Attribution 4.0 International license. Further distribution of this work must maintain attribution to the author(s) and the published article's title, journal citation, and DOI.

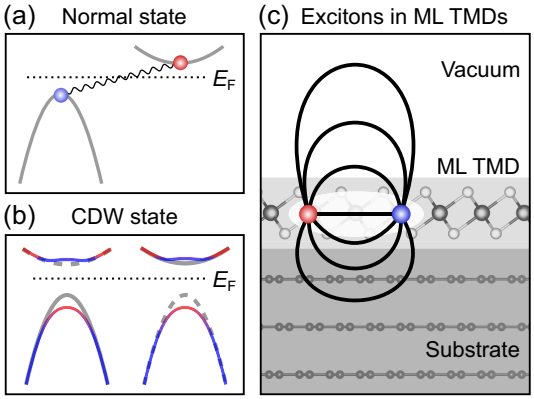


FIG. 1. Electronic structure and ordering instability in $TiSe_2$. (a),(b) Simplified schematic low-energy electronic structure in the (a) normal state and (b) ordered state of $TiSe_2$. The pairing interactions that could mediate this transition in an excitonic insulator model are shown schematically in (a). In (b), solid (dashed) gray lines represent the original (replica) version of the bands in the normal state. The colored lines represent the electronic structure in the ordered state, with blue (red) color indicating the band character of the normal state electron (hole) band. (c) Illustration of reduced screening of the electron-hole interactions in the monolayer limit. The degree of change expected will be modified both by dielectric screening from the encapsulating media and from internal free-carrier screening within the 2D layer itself.

from studies of, e.g., semiconducting WS_2 and $MoSe_2$ that electron-hole interactions can be dramatically enhanced by reduced screening in the 2D limit [see Fig. 1(c)] [19–21], yielding a tuning parameter that is unique to 2D materials. To date, however, it remains unclear whether this provides an effective tuning strategy for the CDW phase in $TiSe_2$: Thickness-dependent studies of exfoliated flakes have yielded contradictory results [22,23], while studies of monolayer (ML) samples are typically conducted on high-screening graphene-based substrates [24–27], finding very similar transition temperatures as for the bulk. Two reports of ML $TiSe_2$ films on weaker-screening MoS_2 substrates [28,29] showcased substantial variations in the claimed transition temperatures, from only a slight increase compared to graphene substrates [29] to a drastic enhancement up to 280 K [28]. This leaves the question of the tunability of the charge-ordered state in $TiSe_2$ via dielectric screening open.

II. HYBRID EXFOLIATION EPITAXY OF ML $TiSe_2$-BASED VAN DER WAALS HETEROSTRUCTURES

In order to realize an optimal low-screening environment for ML $TiSe_2$, it should be fabricated on an insulating support substrate. The "gold-standard" material for this purpose is hexagonal boron nitride (*h*-BN), with a static out-of-plane dielectric constant of $\varepsilon \approx 3$–4 [30–32] which is significantly lower even than that of the semiconductor MoS_2 used as a substrate in previous studies [28,29] ($\varepsilon \approx 7$–8 [31,33]). However, this presents two significant experimental challenges. (1) ML $TiSe_2$ has never been realized via mechanical exfoliation, with exfoliated samples in the literature typically having thicknesses on the order of 5–10 nm [34]. Instead, ML $TiSe_2$ samples are typically fabricated via molecular-beam epitaxy [25,26,35,36]. Obtaining high-quality epitaxial transition-metal dichalcogenide (TMD) layers on *h*-BN substrates is notoriously challenging due to the sluggish growth kinetics and lack of unsaturated dangling bonds on the substrate surface, typically leading to undesirable growth morphologies and premature onset of bilayer formation [37]. (2) Arguably the most effective route to investigate the phase transition in the monolayer limit of $TiSe_2$ is via the corresponding evolution of its electronic structure, as probed by angle-resolved photoemission (ARPES). However, ARPES cannot typically be performed on insulators like *h*-BN.

To overcome both of these challenges, we have developed a hybrid bottom-up and top-down fabrication procedure, as outlined in Fig. 2 (see Appendix A for details). Similar fabrication strategies have been employed previously with promising results for the semiconducting TMDs MoX_2 ($X = S$, Se) [38,39]. Thin flakes (several tens of nanometer thickness) of *h*-BN are exfoliated using the Scotch-tape method and transferred onto a conducting 0.5 wt % Nb-doped TiO_2 substrate [Fig. 2(a)]. Such flakes are thin enough that the photoinduced current across the flake is sufficient to allow ARPES measurements with only a small influence of charging [40,41]. Next, a monolayer of $TiSe_2$ is grown on the substrate by molecular-beam epitaxy (MBE); see Fig. 2(b). To overcome the challenges of *h*-BN as a growth substrate, we use our recently developed method for nucleation-assisted MBE growth of 2D materials [42], which allows us to fabricate a uniform monolayer with near complete coverage and negligible bilayer regions (see Fig. 1 in Supplemental Material for additional materials characterization [43]). Because of the small lateral size of the exfoliated *h*-BN flakes (typically on the scale of a few 10 μm), electronic structure measurements of the resulting ML $TiSe_2$/*h*-BN heterostructures necessitate microfocus (μ)-ARPES experiments with a beam spot focused down to ~10 μm [Fig. 2(c); see also Appendix A]. This provides sufficient spatial resolution to probe the ML $TiSe_2$/*h*-BN heterostructure, while still allowing good spectral resolution for studying the electronic states of interest: As shown in Figs. 2(d) and 2(e), the *h*-BN flakes can be readily located from the integrated ARPES contrast in spatial mapping data, due to the distinct photoemission intensity between spectra measured from atop the *h*-BN flake and on the TiO_2 substrate. Comparing the μ-ARPES spectra off and on the flake [Fig. 2(f)], it is clear that high-quality band dispersions of ML $TiSe_2$ are

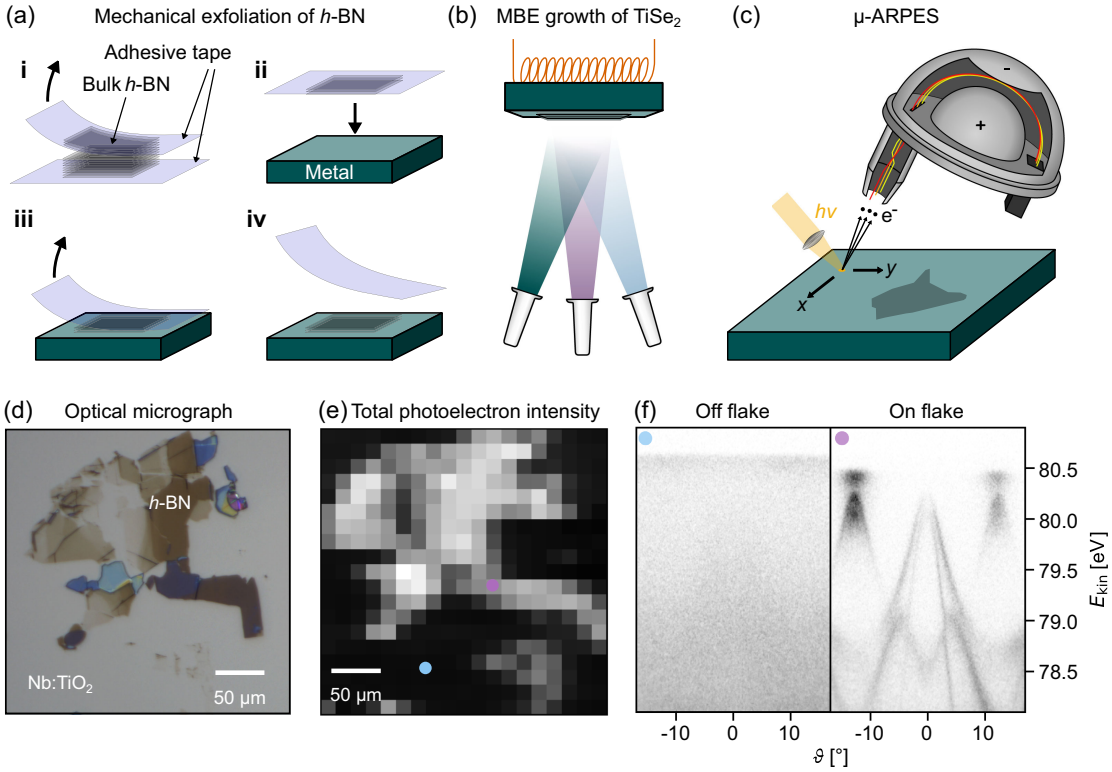


FIG. 2. ML $TiSe_2/h$-BN heterostructures. (a)–(c) Fabrication and characterization. (a) h-BN bulk crystals are exfoliated to flakes with a thickness of several tens of nanometers, which are then transferred on to a conducting substrate; (b) monolayer films of $TiSe_2$ are grown atop the h-BN flakes by molecular beam epitaxy; (c) electronic structure measurements of the $TiSe_2/h$-BN heterostructures are enabled by μ-ARPES. (d) Optical micrograph of h-BN flakes on a conducting Nb:TiO_2 substrate. (e) Spatial map of integrated photoemission intensity in the region around the large flake shown in (d). (f) Representative photoemission measurements performed with the beam located off (left) and on (right) the h-BN flake. High-quality ARPES spectra of ML $TiSe_2$ are obtained only from atop the h-BN surface.

obtained from atop, and only atop, the h-BN. These are almost free from charging effects, as evident from the fact that the Fermi levels are nearly aligned in the two measurements shown. Off the flake, only diffuse photoemission signal is obtained, indicating that a well-ordered $TiSe_2$ film is only present on the h-BN flakes. We choose a thicker region (≈65 nm) of the h-BN flake for further measurements, since the surface roughness in thinner areas typically impairs the $TiSe_2$ film quality. This thickness is also sufficient for the flake to be considered as bulklike in terms of dielectric screening at the surface [44].

III. INFLUENCE OF GROWTH SUBSTRATE ON THE GROUND STATE ELECTRONIC STRUCTURE

Our hybrid fabrication approach opens the door to a systematic investigation of the effect of the substrate screening on the electronic structure of $TiSe_2$ by comparing to measurements of more conventional $TiSe_2$/graphite reference samples. We show measurements of the ground-state electronic structure of these systems in Fig. 3. In both cases, the well-known dispersion of ML $TiSe_2$ is obtained, with a pair of spin-orbit-split Se $4p$-derived valence bands at the Γ point, Ti$3d$-derived electron pockets located in the vicinity of the Fermi level at the M points, and strong replicas of the valence band below the Ti conduction bands. The similar electronic structure suggests weak direct hybridization between the substrate and epilayer states, consistent with the insulating nature of h-BN, and the limited k-space extent of the graphite states near the Fermi level. The replica bands provide a particularly clear and characteristic spectroscopic signature of the CDW state, and arise due to a backfolding of the valence bands by the 2×2 periodic lattice distortion that accompanies the CDW (see Ref. [26] for a detailed discussion of the ground-state electronic structure).

While the band features are qualitatively consistent for the samples grown on different substrates, several differences are evident. Spectral features appear broader in the case of the $TiSe_2/h$-BN sample, which we attribute to slight residual charging due to the insulating nature of h-BN (see also Appendix A 2). Furthermore, the spectra from the sample on graphite exhibit nearly symmetric intensity in k_x, while we observe a clear asymmetry between the backfolded states at the M points located at

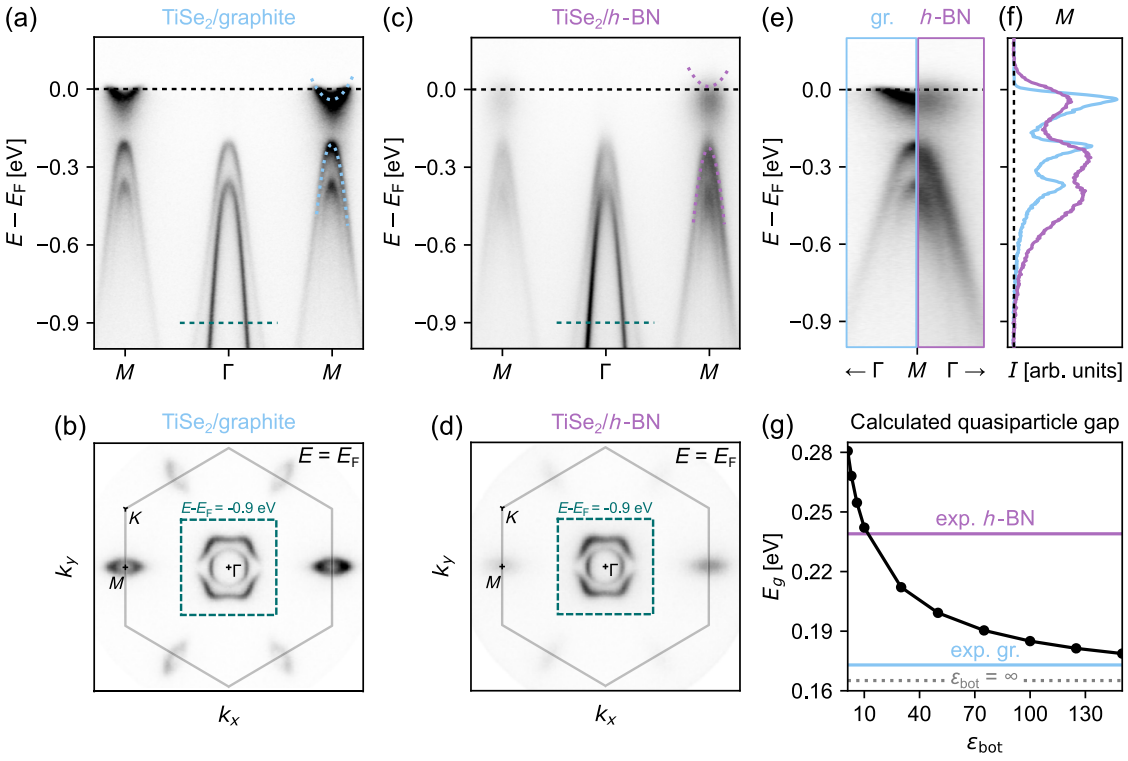


FIG. 3. Low temperature electronic structure measurements of $TiSe_2/h$-BN and $TiSe_2$/graphite heterostructures. (a) Band dispersion and (b) constant energy contours at the Fermi level for monolayer $TiSe_2$/graphite, measured at $T = 18$ K. The dashed region in (b) shows a constant energy contour at a binding energy of 0.9 eV, showing the valence band [see dashed horizontal line in (a)]. (c),(d) Equivalent spectra measured on $TiSe_2/h$-BN. (e) Direct comparison of conduction and valence band spectra at the M point, and (f) corresponding EDCs at the M point. (g) Calculated dependence of the quasiparticle band gap of ML $TiSe_2$ on the dielectric environment. $\varepsilon_{\mathrm{bot}}$ is the dielectric constant of the semi-infinite space below the $TiSe_2$ layer. The purple and blue lines indicate the quasiparticle gaps for ML $TiSe_2$ on h-BN and graphite substrates as determined from our experimental ARPES data, and the gray line is the calculated limit for $\varepsilon_{\mathrm{bot}} = \infty$.

positive and negative momentum for the sample on h-BN. We assign this to the suppression of twin domains in the growth of the $TiSe_2$ film on h-BN, due to the threefold symmetry of the h-BN surface as compared to the sixfold symmetry of a graphene layer. More importantly, while the spectra in the graphite case show strong, well-defined elliptical conduction pockets with a conduction band minimum located approximately 40 meV below the Fermi level, we observe faint tails of the conduction band minimum only in the case of the h-BN substrate. From two-dimensional fits of the spectral function (see Fig. 2 in Supplemental Material [43]), we estimate that the conduction band minimum is located (12 ± 15) meV above the Fermi level for ML $TiSe_2/h$-BN.

Notably, in contrast to previous measurements of monolayer $TiSe_2$, our constant energy contours in Figs. 3(b) and 3(d) are free from rotational disorder. For the sample on a graphite substrate, the well-developed Fermi contours allow making a precise quantification of the free-carrier density of $(3.0 \pm 0.1) \times 10^{13}$ e^-/cm^2 in the $TiSe_2$ layer from a Luttinger analysis. The carrier density is clearly significantly lower for the sample grown on h-BN. Given the difficulty of precisely locating its essentially unoccupied conduction band, we estimate the carrier density by assuming the Fermi level sits 3 meV above the bottom of the band—the most occupied value allowed by the error bars of our 2D fitting analysis. This yields a generous upper limit of the carrier density for our ML $TiSe_2/h$-BN of 3×10^{12} e^-/cm^2, i.e., at least an order of magnitude lower than for the sample on graphite.

While it was previously suggested that off stoichiometries may be responsible for the electron doping of monolayer $TiSe_2$ films [25], the low concentrations of Se vacancies found in sister samples to those studied here [42] cannot account for the doping level present in the $TiSe_2$/graphite sample. Furthermore, the samples on both growth substrates were grown under the same conditions (substrate temperature, metal, and chalcogen flux), and so could be expected to have equivalent vacancy concentrations. We therefore attribute the increased carrier doping in $TiSe_2$/graphite as an influence of intrinsic charge transfer from the semimetallic graphite substrate to the $TiSe_2$ layer atop.

Crucially, this leads to a situation here where *both* the dielectric screening from the substrate as well as the

internal screening from free carriers in the $TiSe_2$ layer itself are reduced for the $TiSe_2/h$-BN heterostructure as compared to the $TiSe_2$/graphite heterostructure. Interestingly, we find that the quasiparticle band gap is larger for $TiSe_2/h$-BN than for $TiSe_2$/graphite. If the change in band filling led simply to a rigid shift of the chemical potential, all states would move to lower binding energy. Figures 3(e) and 3(f), however, show that the valence bands are shifted to higher binding energy for $TiSe_2/h$-BN, despite the smaller filling of the conduction band. From our fits (Fig. 2 in Supplemental Material [43]) we find that the band gap in $TiSe_2/h$-BN is (239 ± 15) meV, while that for $TiSe_2$/graphite is (173 ± 6) meV, nearly 30% smaller.

In doped semiconductors, it is well established that the increased screening from induced free carriers can lead to a reduction in the quasiparticle band gap with increasing carrier density [45,46], an effect which can be particularly pronounced in the semiconducting TMDs [47–52]. To confirm whether substrate screening could also drive the band gap changes observed here, we estimate the quasiparticle band gap E_g for different substrate dielectric constants $\varepsilon_{\mathrm{bot}}$, using a model based on a Wannierized density functional theory (DFT) band structure [53] with corrections from the Coulomb hole plus screened exchange (COHSX) approximation (neglecting spin-orbit coupling for simplicity; see Appendix A 3). As shown in Fig. 3(g), we find a significant enhancement of E_g as the environmental screening is reduced from a metallic ($\varepsilon_{\mathrm{bot}} = \infty$) to an insulating substrate (lower $\varepsilon_{\mathrm{bot}}$; see also Fig. 3 in Supplemental Material [43]). Using a realistic value of $\varepsilon_{\mathrm{bot}} = 3$ to represent the h-BN substrate and $\varepsilon_{\mathrm{bot}} = \infty$ to represent the graphite substrate, we find band gaps of 268 and 162 meV, respectively, which are comparable to the respective experimentally observed gaps. While taking $\varepsilon_{\mathrm{bot}} = \infty$ for the graphite substrate is an idealized approximation, any $\varepsilon_{\mathrm{bot}} \gg 3$ yields a band gap that is significantly reduced compared to the h-BN case (see also Appendix A 5), such that we attribute the change of band gap predominantly to an environmental screening-induced modification of the Coulomb-driven band gap renormalization. Together, our theoretical and experimental findings thus indicate that our samples grown on different substrates are susceptible to "Coulomb engineering" [54–56] of their electronic states.

IV. TEMPERATURE-DEPENDENT EVOLUTION OF ELECTRONIC STRUCTURE

To investigate whether this has any influence on the phase transition in $TiSe_2$, we have performed temperature-dependent measurements of the electronic structure. Figure 4(a) shows the measured dispersions from $TiSe_2/h$-BN (see Fig. 4 in Supplemental Material for the equivalent measurements of $TiSe_2$/graphite [43]). With increasing temperature, we observe a monotonic reduction of the spectral weight of the replica states at the M points, indicating the suppression of the CDW order at higher temperatures. This is also apparent from the energy distribution curves (EDCs) extracted at the M point, while EDCs taken at the Γ point indicate a small temperature-dependent shift of the top of the valence band to higher binding energies with decreasing temperature [Fig. 4(b)]. Intriguingly, while the replica states lose sharpness at 200 K, significant spectral weight persists to room temperature and beyond. However, precursor fluctuations of the order parameter can persist well above T_c for a strong-coupling transition, where they are known to cause remnant CDW-like signatures including replica spectral weight and even hybridization gaps [4,57]. Furthermore, the features observed from $TiSe_2/h$-BN are all qualitatively similar to those observed from our companion samples grown on graphite substrates [Fig. 4(c); see also Fig. 4 in Supplemental Material] as well as previous measurements for samples on graphene substrates (Refs. [26,35]).

To assess whether there are any signatures of differences in the ordering instability for $TiSe_2/h$-BN and $TiSe_2$/graphite, we therefore perform two separate quantitative analyses of the temperature-dependent ARPES data. First, we fit the valence band positions extracted from temperature-dependent EDCs at Γ [Fig. 4(d)], searching for the onset of shifts due to band hybridization at the CDW transition [26]. While the band positions for $TiSe_2/h$-BN are offset to slightly higher binding energies than for $TiSe_2$/graphite, reflecting the larger quasiparticle gap of the former as discussed above, both systems present a nearly indistinguishable temperature evolution. Crucially, both show a change of slope at ~200 K, suggesting that both share a very similar CDW transition temperature to that of the bulk. Second, we quantify the evolution of the replica spectral weight via a region of interest (ROI) analysis [see dashed lines in Fig. 4(a) and Appendix A for details]. From Fig. 4(e), it is clear that both $TiSe_2/h$-BN and $TiSe_2$/graphite exhibit an essentially identical CDW behavior. For both, we observe significant replica weight persisting to our highest measurement temperatures of 380 and 360 K, respectively indicative of strong CDW fluctuations (see also Fig. 5 in Supplemental Material [43]). A subtle change of slope at $T \approx 200$ K again indicates a phase transition close to the bulk $TiSe_2$ value of 202 K [7] in both ML $TiSe_2/h$-BN and ML $TiSe_2$/graphite. In fact, the persistence of replica weight above the CDW transition is arguably even more evident in the case of graphite [see Fig. 4(c)], where weak valence band peaks are visible in the EDCs at M up to 300 K.

V. DISCUSSION AND PERSPECTIVES

Our observation of a large band gap renormalization of the $TiSe_2$ states of >60 meV indicates a significant influence of dielectric screening by the graphite substrate and by the free carriers within the $TiSe_2$ layer itself. Indeed, the free-carrier density in the $TiSe_2$ layer for our

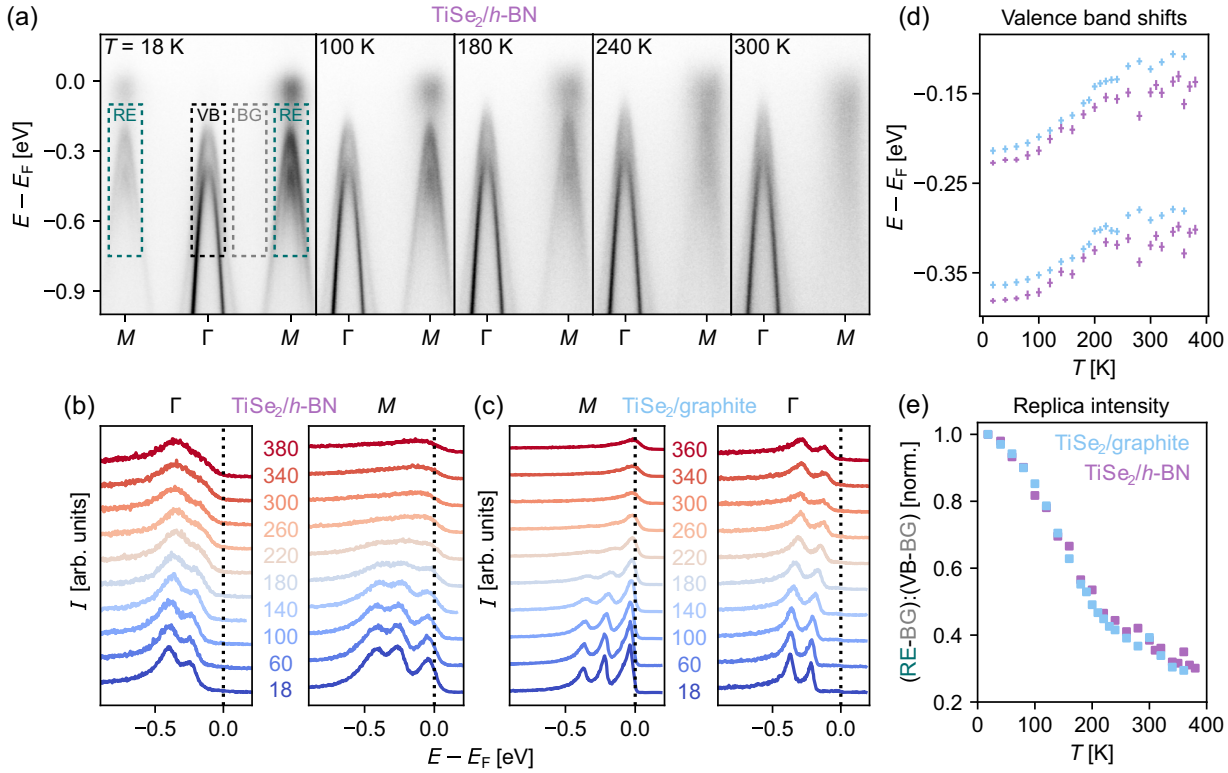


FIG. 4. Temperature-dependent electronic structure of $TiSe_2/h$-BN as compared to $TiSe_2$/graphite. (a) Band dispersions of $TiSe_2/h$-BN taken at selected temperatures across the CDW transition. (b),(c) EDCs at selected temperatures for (b) $TiSe_2/h$-BN and (c) $TiSe_2$/graphite, showing suppression of replica peaks and valence band shifts. (d) Temperature-dependent evolution of the valence band positions, showing the onset of valence band hybridization at the CDW transition and (e) evolution of the CDW replica intensity. VB, BG, and RG are the integrated intensities of the valence bands, background and replica states, respectively, as marked in (a). Both the band positions and replica intensities show temperature-dependent trends which show negligible dependence on the substrate.

$TiSe_2$/graphite heterostructures is comparable to the exciton Mott density observed in well-known large-gap semiconducting TMDs even in low-screening environments [48,58–60]. In combination with the extrinsic screening from the graphite substrate [59], we thus conclude that our ML $TiSe_2$/graphite sample is well above the Mott transition and excitons therefore cannot play any significant role in driving a CDW phase transition in this sample. Yet, its temperature-dependent electronic structure evolution is virtually indistinguishable from that of $TiSe_2/h$-BN, while the extracted transition temperatures are within experimental error of one another, and of the bulk.

Our measurements thus directly indicate that excitons are not required to obtain the well-known CDW phenomenology of $TiSe_2$, pointing to a core importance of electron-phonon coupling. Indeed, environmental screening predominantly affects quantities in the long-wavelength limit, i.e., at small scattering wave vectors $\mathbf{q}$ close to Γ, as described by Eq. (A2). The dominant contribution to the electron-phonon coupling vertex is not at $\mathbf{q} = \Gamma$, however, but rather at larger wave vectors that connect the Γ and M pockets of the Fermi surface [61]. As a consequence, we would not expect Coulomb engineering to significantly affect the electron-phonon coupling vertex in monolayer $TiSe_2$.

To further explore why the electronic structure is sensitive to Coulomb engineering, but the CDW formation is not, we consider a simplified model consisting of two orbitals with energies ε_c and ε_v, representing the conduction band with Ti-d character and the valence band with Se-p character, respectively [Fig. 5(a)]. The minimal Hamiltonian takes the form

$$H = \sum_{\sigma,\alpha} \varepsilon_\alpha n_{\alpha,\sigma} + W \sum_{\alpha} n_{\alpha,\uparrow} n_{\alpha,\downarrow} + W' \sum_{\sigma,\sigma'} n_{c,\sigma} n_{v,\sigma'}, \quad (1)$$

where $\alpha \in \{c, v\}$, $\sigma, \sigma' \in \{\uparrow, \downarrow\}$, and $n_{\alpha,\sigma}$ denotes the density operator. We set the single-particle energies of the Ti and Se orbitals to $\varepsilon_c = 88$ meV and $\varepsilon_v = -12$ meV, respectively. From the modeling of the quasiparticle band structure we define the intraorbital interaction as $W = \sum_{\mathbf{q}} W_{\mathrm{TiTi}}(\mathbf{q})$, the interorbital interaction as $W' = \sum_{\mathbf{q}} W_{\mathrm{TiSe}}(\mathbf{q})$, and assume all other Coulomb matrix elements to be zero. In Fig. 5(b) we show how W and W', as well as their difference $W - W'$, depend on the substrate dielectric constant $\varepsilon_{\mathrm{bot}}$. Notably, the dipole term $W - W'$ is relatively weakly dependent on $\varepsilon_{\mathrm{bot}}$ as compared to the monopole terms W and W'. In order to estimate the

effect of the substrate on CDW formation, we consider the phonon softening described by the following phonon self-energy in the static limit,

$$\Pi(\mathbf{q}, \omega = 0) = g^2 \chi(\mathbf{q}, \omega = 0) \propto \frac{g^2}{\Delta_c}, \tag{2}$$

where g is the electron-phonon coupling vertex and $\chi(\mathbf{q}, \omega = 0)$ is the charge susceptibility [62]. Here, we have inserted the charge susceptibility evaluated in our simple model at zero temperature, where Δ_c is the cost of electron-hole excitations (see Appendix A 4). From the above expression we understand that the phonon self-energy that is necessary for the CDW formation is inversely proportional to Δ_c, such that in the following we can limit our discussion to the dependence of Δ_c on environmental screening. We have furthermore neglected dynamical screening, which we discuss in more detail in Appendix A 6.

To this end, we closely follow Ref. [63] and consider the electron configurations shown in Fig. 5(a). In the ground state E_1, the Se orbital is completely filled and the Ti orbital is completely empty. Removing or adding an electron from this state yields energies E_2 and E_3, respectively. An estimate for the electronic quasiparticle gap E_g as probed in ARPES is then the difference between the electron ionization $(E_2 - E_1)$ and affinity $(E_1 - E_3)$ energy, such that

$$\begin{aligned} E_g &= (E_2 - E_1) - (E_1 - E_3) \\ &= \varepsilon_c - \varepsilon_v - (W - W') + W'. \end{aligned} \tag{3}$$

The cost of a particle-hole excitation $\Delta_c = E_4 - E_1$ is

$$\Delta_c = \varepsilon_c - \varepsilon_v - (W - W') < E_g, \tag{4}$$

which is smaller than the quasiparticle gap E_g as a consequence of the attractive interaction between the electron and the hole [63]. This yields an estimate for the exciton binding energy given by

$$E_{\text{ex}} = E_g - \Delta_c = W'. \tag{5}$$

We note that, in our minimal model, the kinetic contributions of E_g and Δ_c cancel, yielding an expression for E_{ex} which is independent of the kinetic energy. If we were to do a full *ab initio* treatment, which includes additional bands as well as their dispersive nature, the kinetic energy contribution would most likely not completely cancel. Nonetheless, our minimal model captures the trends of experiments and sophisticated *ab initio* calculations of the lowest exciton of transition metal dichalcogenide semiconductors, such as a weak sensitivity of the excitation energy and a strong sensitivity of the exciton binding energy to Coulomb engineering [55,64,65]. It is therefore sufficient to develop a qualitative understanding of the effects of Coulomb engineering here.

To this end, we show E_g, Δ_c, and E_{ex} as a function of ε_{bot} in Fig. 5(c) [note that the values of E_g are different from those in Fig. 3(g) due to the simplified model used here]. We find that both the quasiparticle gap E_g and the exciton binding energy E_{ex} are efficiently tuned by Coulomb engineering following essentially W'. Interestingly, we find that this tunability is not reflected by the cost of particle-hole excitations Δ_c, where both W' dependencies cancel out and only the weaker dependence of the dipole term $\sim(W - W')$ enters. As a result, Δ_c is only weakly dependent on ε_{bot}. The transition to the CDW phase should therefore be relatively insensitive to Coulomb engineering because the screening effects on E_g and E_{ex} mostly cancel each other. The relative excitonic contribution to Δ_c can therefore be tuned by changing the screening. This leaves the intriguing situation where some excitonic contributions can occur in the h-BN-supported case, yet yielding the same T_{CDW} as for the graphite-supported case where we have shown that the phase transition occurs even without an excitonic contribution.

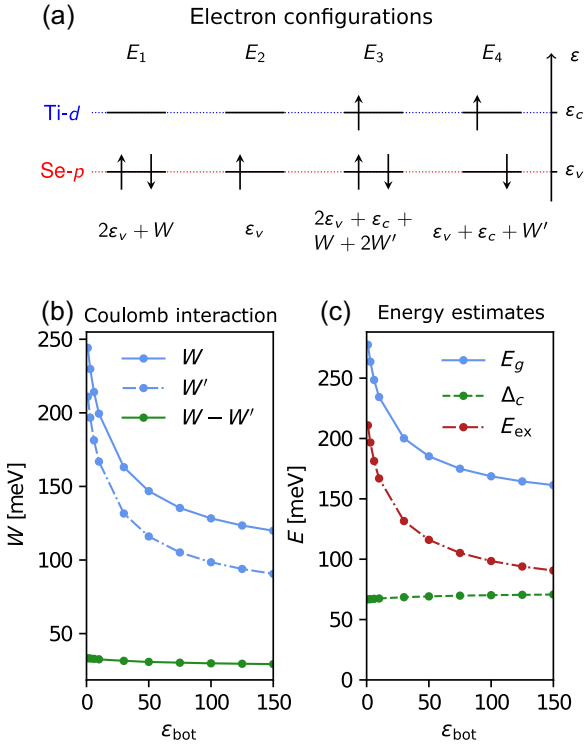


FIG. 5. Theoretical modeling of exciton binding energies. (a) Schematic of four relevant electron configurations E_1–E_4 in a two-orbital model, with their corresponding energies denoted underneath. (b) Theoretical estimates of the intraorbital and interorbital screened Coulomb interactions W and W', as well as their difference $W - W'$, as a function of the substrate dielectric constant ε_{bot} (see Appendix A 6 for a discussion of dynamical effects). (c) Corresponding estimates for the quasiparticle gap E_g, particle-hole excitation energy Δ_c, and exciton binding energy E_{ex}.

While our study therefore shows that excitonic contributions to the phonon softening can be effectively tuned by Coulomb engineering here, it also directly indicates that the CDW remains stable when these are suppressed, realizing an intriguing, but ultimately conventional, charge-density wave in $TiSe_2$. This finding is in good agreement with very recent high-fidelity electronic structure calculations for bulk $TiSe_2$, performed using quasiparticle self-consistent *GW* calculations which were extended to include ladder diagrams in the screened Coulomb interaction [4]. These point to a negligible contribution of electron-hole interactions in the higher screening environment of the bulk system. Moreover, using molecular dynamics calculations, they predicted that lattice fluctuations can produce significant CDW-like signatures even at room temperature, far above the CDW transition [4]. This has also been observed experimentally in bulk $TiSe_2$ [66] and is again in excellent agreement with our observation of persistent backfolded spectral weight to temperatures of approximately twice T_c in our experimental measurements. We hope that our work here will motivate similar experimental studies of the electron dynamics and state-of-the-art *ab initio* theoretical studies also for monolayer $TiSe_2$.

We note that multiple systems have been proposed in recent years as putative excitonic insulator candidates [67–74], several based on their similarity to the electronic structure of $TiSe_2$ [71–73]. Our results here suggest that extreme care should be taken when assigning capacity to host the exciton insulator phase based on band structure arguments alone. More broadly, our results directly demonstrate the Coulomb engineering of the electronic structure of $TiSe_2$, allowed by our hybrid exfoliation-epitaxy materials advance. This, in turn, opens the exciting prospect for deterministically modifying long-range Coulomb interactions for tuning the many-body states and phases of a broad array of 2D quantum materials.

ACKNOWLEDGMENTS

We thank Matt Watson and Peter Wahl for useful discussions. We gratefully acknowledge support from the Engineering and Physical Sciences Research Council (under Grants No. EP/X015556/1, No. EP/T02108X/1, and No. EP/M023958/1) and the Leverhulme Trust (Grant No. RL-2016-006). We gratefully acknowledge MAX IV Laboratory for time on the Bloch beam line under Proposals No. 20220959, No. 20230206, and No. 20231118. Research conducted at MAX IV, a Swedish national user facility, is supported by the Swedish Research council under Contract No. 2018-07152, the Swedish Governmental Agency for Innovation Systems under Contract No. 2018-04969, and Formas under Contract No. 2019-02496. Y. V. and T. W. acknowledge funding by the Cluster of Excellence "CUI: Advanced Imaging of Matter" of the Deutsche Forschungsgemeinschaft (DFG) (EXC 2056, Project No. 390715994) and the DFG research unit FOR 5249 ("QUAST," Project No. 449872909). J. B. acknowledges funding by the DFG under Germany's Excellence Strategy [University Allowance, (EXC 2077, Project No. 390741603, University of Bremen)].

DATA AVAILABILITY

The research data supporting this publication can be accessed at [75].

APPENDIX: METHODS

1. Sample preparation

For the *h*-BN substrates, *h*-BN flakes were mechanically exfoliated from bulk crystals (purchased from hqgraphene) using Nitto wafer tape, and directly transferred to a 0.5 wt % $Nb:TiO_2$ substrate (purchased from Shinkosha). Exfoliation and transfer were conducted in a glove box under a N_2 atmosphere. The substrates were then cleaned using acetone and isopropanol before loading them into the ultrahigh vacuum (UHV) system. For the graphite substrates, natural graphite single crystals purchased from NGS Naturgraphit were used. For easier mounting, the crystals were glued onto tantalum chips using high temperature carbon paste and annealed in a separate vacuum chamber at 700 °C and $\sim 10^{-8}$ mbar for several hours to outgas the glue. The graphite crystals were then cleaved in air using adhesive tape and immediately loaded into the UHV system for film deposition. All substrates were annealed in the load lock of the UHV system at 200 °C for ∼10 h and again in the MBE chamber at 700 °C–800 °C directly before the growth. The freshly cleaved graphite crystals were annealed for ∼30 min whereas the *h*-BN substrates were annealed for at least 1 h and always at 800 °C in order to minimize any impurities from the mechanical exfoliation.

The film growth was conducted using the nucleation-assisted growth mode described in Ref. [42]. During the growth, the samples were held at 550 °C with a Se beam equivalent pressure of 2×10^{-7} mbar. After growth, the samples on *h*-BN substrates were annealed under this Se pressure and at growth temperature for up to 1 h. Finally, they were cooled down from growth temperature at 20 K/ min and the Se flux was shut at 260 °C. For samples grown on graphite substrates, postgrowth annealing leads to excessive monolayer to bilayer conversion, and so the samples were directly cooled down under Se flux. For a near complete monolayer, the growth time on *h*-BN was 2 h 40 min and on graphite 1 h 5 min. The base pressure of the growth chamber was 2×10^{-10} mbar and typical background pressures during the deposition are $(2–4) \times 10^{-9}$ mbar.

After the growth, the samples were capped with a ∼5-nm-thick layer of amorphous Se, deposited at room temperature. This acted as a protective cap for transporting the samples through air for the ARPES measurements.

The cap was removed *in situ* in the measurement system by mild annealing at 265 °C for 1 h. This decapping procedure was optimized based on XPS measurements of the Se3*d* core level (see Fig. 1 in Supplemental Material [43]). The decapping temperature was monitored with a thermocouple located next to the sample plate, and the pressure during decapping was kept below 1×10^{-9} mbar.

We note that, for the samples grown on *h*-BN, we observed some variation of the photoemission signal strength, background intensity, and signatures of domain twinning depending on the flake thickness. This likely reflects a dependence of the film growth quality on the thickness of the *h*-BN flake: With decreasing flake thickness, the *h*-BN surface inherits a higher roughness from the TiO_2 substrate, reducing adatom diffusion during the growth and impairing the film quality. We have found that we generally observe the highest spectral quality for flake thicknesses $\gtrsim$50 nm, where the surface is sufficiently flat for unperturbed film growth. For the regions investigated here, we estimate an *h*-BN flake thickness of ∼65 nm based on optical contrast and color of the flake regions. It is known that in *h*-BN and heterostructures with ML TMDs the screening of excitons rapidly approaches bulklike levels from a thickness of few nanometers [44], and so the *h*-BN flakes can be considered effectively bulklike here.

2. ARPES

ARPES experiments were performed at the Bloch A-branch end station of the MAX IV synchrotron, Lund, Sweden. A photon energy of 85 eV and linear vertical polarization was used in all measurements, which we found maximized the spectral weight at the top of the valence band, due to photoemission matrix element variations. For Fermi level referencing of the samples grown on *h*-BN, which still exhibited a small amount of charging, we measured the Se3*d* core levels together with each valence spectrum across the temperature series. To avoid changing the beam flux on the sample, these were measured using the second harmonic of the core 85 eV photons. The Fermi level was determined for the base temperature spectrum by fitting of a Fermi function to the data, with the Fermi level for the higher temperature spectra then calculated based on the shift of the Se core levels across the temperature series.

The residual charging leads to a small additional broadening of the measured spectra. We accounted for this in our quantitative analysis using a Gaussian convolution in energy. For our fits to the samples on *h*-BN, we use a Gaussian with standard deviation $\sigma = 40$ meV which accounts for the charging contribution in addition to our experimental energy resolution of $\sigma \approx 7$ meV. For the samples on graphite, a narrower Gaussian with $\sigma = 9$ meV is used.

To correct for thermal drift of the samples, we performed spatial reregistration using ARPES-based spatial mapping. We found that the degree of twin domain formation showed some spatial variations on the sample, leading to a change in relative intensity at positive and negative momenta. To rule out any influence of this for our spectral weight analysis, we thus performed the ROI analysis by taking the average of the integrated intensity of the backfolded weight at positive and negative momenta. We then subtracted the background intensity and normalized the intensity to the background-corrected value to obtain the replica intensity reported in Fig. 4(e).

For the estimation of the free-carrier density in $TiSe_2$/*h*-BN, we assume a nearly free-electron-like dispersion of the conduction band with an effective mass based on the $TiSe_2$/graphite data.

ARPES data analysis was performed using the PEAKS package [76].

3. Quasiparticle band gap

For the theoretical modeling of the Coulomb engineering of the band gap, we start from the Wannierized density functional theory band structure of ML $TiSe_2$ in Ref. [53]. It is constructed from 5 Ti 3*d* orbitals and 2×3 Se 4*p* orbitals, which together dominantly contribute to the bands around the Fermi energy. Since we are mostly interested in qualitative changes of the band structure due to the substrate, we will neglect spin-orbit coupling to reduce computational cost. DFT predicts ML $TiSe_2$ to be metallic due to the well-known band gap problem of semilocal DFT functionals. To correct for this, we use the scissor operator to introduce a gap of 0.1 eV (i.e., by shifting the Ti *d* and Se *p* orbitals up and down in energy, respectively), leading to the band structure shown in Fig. 3 in Supplemental Material [43].

To analyze the effect of Coulomb engineering, we augment this model with Coulomb interactions. The bare Coulomb interaction in the density-density approximation is written as

$$V_{\alpha\beta}(\mathbf{q}) = \frac{2\pi e^2}{Aq} e^{-i\mathbf{q}\cdot\boldsymbol{\tau}_{\alpha\beta}} e^{-qd_{\alpha\beta}}, \tag{A1}$$

where $\boldsymbol{\tau}_{\alpha\beta}$ is the in-plane distance between orbitals α and β, and $d_{\alpha\beta}$ the corresponding out-of-plane distance. For simplicity, we set the orbital positions to the positions of the corresponding atoms. Similar to Ref. [77], we treat screening from the environment, as well as internal screening, by dividing the leading eigenvalue of $V_{\alpha\beta}(\mathbf{q})$ by

$$\varepsilon_{\text{back}}(\mathbf{q}) = \varepsilon_{\text{int}} \frac{1 - \beta_{\text{top}}\beta_{\text{bot}} e^{-2qh}}{1 + (\beta_{\text{top}} + \beta_{\text{bot}}) e^{-qh} + \beta_{\text{top}}\beta_{\text{bot}} e^{-2qh}}, \tag{A2}$$

where $\beta_{\text{top/bot}} = (\varepsilon_{\text{int}} - \varepsilon_{\text{top/bot}})/(\varepsilon_{\text{int}} + \varepsilon_{\text{top/bot}})$, and dividing the subleading eigenvalues by ε_{int}. The resulting screened Coulomb interaction is denoted by $W_{\alpha\beta}(\mathbf{q}, \omega = 0)$. Here we set the internal $TiSe_2$ dielectric constant $\varepsilon_{\text{int}} = 70$. The dielectric constant of the substrate ε_{bot} is set to 3 for $TiSe_2$

mounted on h-BN, or to infinity when mounted on graphite. We set the dielectric constant above the $TiSe_2$ layer to $\varepsilon_{\text{top}} = 1$, representing vacuum, and the effective $TiSe_2$ thickness to $h = 8$ Å.

To qualitatively describe the renormalization of the normal state due to nonlocal Coulomb interactions, we use the Coulomb hole plus screened exchange approximation [78,79]. It is given by the following self-energy in the orbital basis,

$$\Sigma^{\text{COHSX}}_{\alpha\beta}(\mathbf{k}) = -\sum_{\mathbf{k}',i} T_{\alpha i}(\mathbf{k}') T^{\dagger}_{i\beta}(\mathbf{k}') n_F(\xi_{\mathbf{k}',i}) \times W_{\alpha\beta}(\mathbf{k}-\mathbf{k}', \omega = 0) + \frac{1}{2}\delta_{\alpha\beta} \sum_{\mathbf{q}} [W_{\alpha\alpha}(\mathbf{q}, \omega = 0) - U_{\alpha\alpha}(\mathbf{q})], \quad \text{(A3)}$$

where $T_{\alpha i}(\mathbf{k})$ are the unitary transformation matrices that transform the bare electron Hamiltonian to the band basis $\xi_{\mathbf{k},i}$, and $n_F(\varepsilon)$ is the Fermi-Dirac distribution function. The COHSX calculations have been performed using the TRIQS [80] and TPRF [81] code bases, with linearly discretized momentum meshes with 100×100 points.

We show the quasiparticle band structure in the COHSX approximation in Fig. 3 in Supplemental Material [43] for $\varepsilon_{\text{bot}} = 3$ and $\varepsilon_{\text{bot}} = \infty$, representing h-BN and graphite substrates, respectively. We find a rigid upward shift of the conduction band, accompanied by a rigid downward shift of the valence band, due to the effects of the self-energy Σ^{COHSX}. The resulting band gap enhancement is larger for the h-BN substrate than for the graphite substrate as a consequence of the reduced screening, as also shown in Fig. 3(g). While taking $\varepsilon_{\text{bot}} = \infty$ for the graphite substrate is an idealized approximation, we note that E_g rapidly reduces with increasing $\varepsilon_{\text{bot}} > 3$. Therefore, while our quantitative results are affected by the precise choice of ε_{bot}, our qualitative conclusions will not be affected by this.

4. Charge susceptibility

The charge susceptibility,

$$\chi(\omega) = \lim_{\delta\to 0} \sum_{ij} \frac{P_i - P_j}{\omega + i\delta - E_i + E_j} \langle j|\hat{n}|i\rangle\langle i|\hat{n}|j\rangle, \quad \text{(A4)}$$

where E_i and $|i\rangle$ are many-body eigenvalues and eigenstates, respectively, $\hat{n}$ is the density operator, and $P_i = \exp(-\beta E_i)/Z$, with Z the partition function [82]. If the chemical potential is set such that there are two particles in the system and we take the limit of zero temperature, then the numerator $P_i - P_j$ restricts state $|i\rangle$ to the two-particle ground state (i.e., $E_i = E_1$ for the minimal model) and state $|j\rangle$ to a two-particle excited state (i.e., $E_j = E_4$), or vice-versa. Substituting this yields

$$\chi(\omega = 0) \approx \lim_{\delta\to 0} 2 \sum_{ij} \frac{|\langle 4|\hat{n}|1\rangle|^2}{i\delta + E_4 - E_1} \propto \frac{1}{\Delta_c}, \quad \text{(A5)}$$

where the factor of 2 is from spin degeneracy.

5. Nonlocal graphite screening

In the main text we made the approximation $\varepsilon_{\text{bot}} = \infty$ for the graphite substrate. This is an idealized approximation, as in reality screening from graphite is momentum dependent. Here we will discuss the effect of such nonlocality.

Environmental screening dominantly affects the Coulomb interaction in the long-wavelength limit, as described by Eq. (A2). Therefore, it is mostly the $\mathbf{q} \to 0$ limit of the graphite dielectric function that will contribute to screening. If we assume screening from graphite to be given by the Thomas-Fermi dielectric function $\varepsilon_{\text{bot}}(q) = 1 + k_0^2/q^2$, this will yield numbers $\varepsilon_{\text{bot}}(q) \gg \varepsilon_{h\text{-BN}}$ as long as k_0 is larger than all relevant q around 0. To confirm this is the case, we estimate the quantitative effect of nonlocal graphite screening by applying the Thomas-Fermi approximation for $\varepsilon_{\text{bot}}(q)$. We show in Fig. 6 in Supplemental Material the resulting screened local Coulomb interactions [Fig. 6(a)] and energy estimates [Fig. 6(b)] as a function of the Thomas-Fermi wave vector k_0 [43]. We find that the monopole terms W and W', as well as their related energies E_g and E_{ex}, are rather sensitive to the precise value of k_0. If we use the estimate $k_0^{\text{gr}} \approx 0.28$ Å^{-1} for graphite [83], this yields $E_g \approx 186$ meV and $E_{\text{ex}} \approx 115$ meV. When we compare this to the values obtained by setting $\varepsilon_{\text{bot}} = 3$ to describe the h-BN substrate ($E_g \approx 263$ meV and $E_{\text{ex}} \approx 197$ meV), we still find a significant reduction of E_g and E_{ex}, such that our conclusions are not affected. The dipole term $W - W'$ and the related cost of particle-hole excitations Δ_c, on the other hand, have a negligible dependence on k_0. Comparing the idealized $\varepsilon_{\text{bot}} = \infty$ approximation and the Thomas-Fermi approximation yields $\Delta_c \approx 70$ meV and $\Delta_c \approx 72$ meV, respectively (for the h-BN substrate we find $\Delta_c \approx 67$ meV). We have thus shown that while nonlocal screening from graphite might quantitatively affect the quasiparticle gap and exciton binding energy in $TiSe_2$, it will not affect the qualitative trends that our conclusions are based on.

6. Dynamical screening

Here, we address the effect of a frequency-dependent interaction on the excitonic and CDW energetics in $TiSe_2$, as well as its impact on observables. The aim of our theoretical analysis is to give an understanding for why the quasiparticle gap as observed with ARPES is sensitive to Coulomb engineering, whereas the transition to the CDW phase is not. We will therefore focus on the effect of dynamical interactions on *changes* induced by Coulomb engineering. To this end, we separate excitations into two

classes: charged monopole excitations and charge neutral dipolar excitations.

ARPES spectra are obtained from monopolar photoemission excitations, which explains why the quasiparticle gap is efficiently tuned with Coulomb engineering. It is well known that frequency-dependent interactions can induce additional spectral features in the ARPES spectrum, such as kinks around the Fermi surface and/or plasmonic replica features below the conduction band. While these features are indeed sensitive to Coulomb engineering, we do not observe them in our experimental ARPES data for either substrate, such that we conclude that we do not need frequency-dependent interactions to qualitatively explain the trends of the quasiparticle spectrum.

The phonon softening as well as exciton formation are sensitive to dipolar excitations. Therefore, their frequency-dependent features will be even less sensitive to Coulomb engineering than the frequency-dependent features of the ARPES spectra. We thus do not expect major changes to the qualitative trends discussed in the main text. To further illustrate this point we will discuss the effect of a frequency-dependent interaction by making use of the plasmon pole approximation. In this approximation we write for the screened interaction in the density-density approximation $W_{\alpha\beta}(\mathbf{q},\omega) = W_{\alpha\beta}(\mathbf{q},\omega=0) + \Delta W_{\alpha\beta}(\mathbf{q},\omega)$, with the dynamic part given by [84]

$$\Delta W_{\alpha\beta}(\mathbf{q},\omega) = \frac{2a_{\alpha\beta}(\mathbf{q})}{\omega_{\mathbf{q}}}\left(1+\frac{\omega_{\mathbf{q}}^2}{(\omega+i\delta)^2-\omega_{\mathbf{q}}^2}\right). \quad \text{(A6)}$$

Here $\omega_{\mathbf{q}}$ is the plasmon dispersion and $a_{\alpha\beta}(\mathbf{q})$ is the electron-plasmon coupling for two electrons in orbitals α and β interacting via a plasmon mode with transfer momentum $\mathbf{q}$. By taking the limit $\omega\to\infty$ we find that $a_{\alpha\beta}(\mathbf{q}) = \omega_{\mathbf{q}}(V_{\alpha\beta}(\mathbf{q}) - W_{\alpha\beta}(\mathbf{q},\omega=0))/2$, where $V_{\alpha\beta}(\mathbf{q})$ is the bare Coulomb interaction. We then assume that the dynamic part of the Coulomb interaction is dominated by a plasmon mode with a characteristic frequency ω_{pl}, such that we can write the real part of the effective interaction in the minimal model as

$$\Delta W_{\alpha\beta}(\omega) \approx [V_{\alpha\beta} - W_{\alpha\beta}(\omega=0)]\frac{\omega^2}{\omega^2-\omega_{pl}^2}, \quad \text{(A7)}$$

with $V_{\alpha\beta} = \sum_{\mathbf{q}} V_{\alpha\beta}(\mathbf{q})$ and $W_{\alpha\beta}(\omega) = \sum_{\mathbf{q}} W_{\alpha\beta}(\mathbf{q},\omega)$. We find that there can be significant changes to the Coulomb interaction due to dynamic screening, especially for frequencies close to the plasmon frequency ω_{pl}. These changes are responsible for inducing plasmonic kinks and replica features in ARPES spectra. However, we also find that the corrections to the intraorbital ($\alpha=\beta$) and interorbital ($\alpha\neq\beta$) Coulomb interactions have the same dependence on $\varepsilon_{\mathrm{bot}}$ through $V_{\alpha\beta} - W_{\alpha\beta}(\omega=0)$. Therefore, even if the frequency-dependent part were large, we would still expect significant cancellation to occur in the dipole term $W - W'$, such that the weak dependence of the cost of particle-hole excitations Δ_c on the dielectric constant $\varepsilon_{\mathrm{bot}}$ is likely unaffected. This confirms the argument made above, that particle-hole excitations are charge neutral dipolar excitations and are thus relatively insensitive to Coulomb engineering.

[1] H. Cercellier, C. Monney, F. Clerc, C. Battaglia, L. Despont, M. G. Garnier, H. Beck, P. Aebi, L. Patthey, H. Berger, and L. Forró, *Evidence for an excitonic insulator phase in* $1T$-$TiSe_2$, Phys. Rev. Lett. **99**, 146403 (2007).

[2] C. Monney, E. F. Schwier, M. G. Garnier, N. Mariotti, C. Didiot, H. Beck, P. Aebi, H. Cercellier, J. Marcus, C. Battaglia, H. Berger, and A. N. Titov, *Temperature-dependent photoemission on* $1T$-$TiSe_2$*: Interpretation within the exciton condensate phase model*, Phys. Rev. B **81**, 155104 (2010).

[3] M. D. Watson, O. J. Clark, F. Mazzola, I. Marković, V. Sunko, T. K. Kim, K. Rossnagel, and P. D. C. King, *Orbital- and* k_z*-selective hybridization of* Se $4p$ *and* Ti $3d$ *states in the charge density wave phase of* $TiSe_2$, Phys. Rev. Lett. **122**, 076404 (2019).

[4] D. Pashov, R. E. Larsen, M. D. Watson, S. Acharya, and M. van Schilfgaarde, $TiSe_2$ *is a band insulator created by lattice fluctuations, not an excitonic insulator*, npj Comput. Mater. **11**, 152 (2025).

[5] D. Jérome, T. M. Rice, and W. Kohn, *Excitonic insulator*, Phys. Rev. **158**, 462 (1967).

[6] W. Kohn, *Excitonic phases*, Phys. Rev. Lett. **19**, 439 (1967).

[7] F. J. Di Salvo, D. E. Moncton, and J. V. Waszczak, *Electronic properties and superlattice formation in the semimetal* $TiSe_2$, Phys. Rev. B **14**, 4321 (1976).

[8] J. A. Wilson, *Concerning the semimetallic characters of* TiS_2 *and* $TiSe_2$, Solid State Commun. **22**, 551 (1977).

[9] T. Pillo, J. Hayoz, H. Berger, F. Lévy, L. Schlapbach, and P. Aebi, *Photoemission of bands above the Fermi level: The excitonic insulator phase transition in* 1T-$TiSe_2$, Phys. Rev. B **61**, 16213 (2000).

[10] H. P. Hughes, *Structural distortion in* $TiSe_2$ *and related materials-a possible Jahn-Teller effect?*, J. Phys. C **10**, L319 (1977).

[11] K. Rossnagel, L. Kipp, and M. Skibowski, *Charge-density-wave phase transition in* $1T$-$TiSe_2$*: Excitonic insulator versus band-type Jahn-Teller mechanism*, Phys. Rev. B **65**, 235101 (2002).

[12] A. Wegner, J. Zhao, J. Li, J. Yang, A. A. Anikin, G. Karapetrov, K. Esfarjani, D. Louca, and U. Chatterjee, *Evidence for pseudo-Jahn-Teller distortions in the charge density wave phase of* $1t-TiSe_2$, Phys. Rev. B **101**, 195145 (2020).

[13] A. Kogar, M. S. Rak, S. Vig, A. A. Husain, F. Flicker, Y. I. Joe, L. Venema, G. J. MacDougall, T. C. Chiang, E. Fradkin, J. van Wezel, and P. Abbamonte, *Signatures of exciton condensation in a transition metal dichalcogenide*, Science **358**, 1314 (2017).

[14] Z. Lin, C. Wang, A. Balassis, J. P. Echeverry, A. S. Vasenko, V. M. Silkin, E. V. Chulkov, Y. Shi, J. Zhang, J. Guo, and

X. Zhu, *Dramatic plasmon response to the charge-density-wave gap development in* 1*T*-$TiSe_2$, Phys. Rev. Lett. **129**, 187601 (2022).

[15] T. Rohwer, S. Hellmann, M. Wiesenmayer, C. Sohrt, A. Stange, B. Slomski, A. Carr, Y. Liu, L. M. Avila, M. Kalläne *et al.*, *Collapse of long-range charge order tracked by time-resolved photoemission at high momenta*, Nature (London) **471**, 490 (2011).

[16] M. Porer, U. Leierseder, J.-M. Ménard, H. Dachraoui, L. Mouchliadis, I. Perakis, U. Heinzmann, J. Demsar, K. Rossnagel, and R. Huber, *Non-thermal separation of electronic and structural orders in a persisting charge density wave*, Nat. Mater. **13**, 857 (2014).

[17] C. Monney, M. Puppin, C. W. Nicholson, M. Hoesch, R. T. Chapman, E. Springate, H. Berger, A. Magrez, C. Cacho, R. Ernstorfer, and M. Wolf, *Revealing the role of electrons and phonons in the ultrafast recovery of charge density wave correlations in* 1*T*-$TiSe_2$, Phys. Rev. B **94**, 165165 (2016).

[18] F. Kurtz, T. N. Dauwe, S. V. Yalunin, G. Storeck, J. G. Horstmann, H. Böckmann, and C. Ropers, *Non-thermal phonon dynamics and a quenched exciton condensate probed by surface-sensitive electron diffraction*, Nat. Mater. **23**, 890 (2024).

[19] Z. Ye, T. Cao, K. O'Brien, H. Zhu, X. Yin, Y. Wang, S. G. Louie, and X. Zhang, *Probing excitonic dark states in single-layer tungsten disulphide*, Nature (London) **513**, 214 (2014).

[20] A. Chernikov, T. C. Berkelbach, H. M. Hill, A. Rigosi, Y. Li, B. Aslan, D. R. Reichman, M. S. Hybertsen, and T. F. Heinz, *Exciton binding energy and nonhydrogenic Rydberg series in monolayer* WS_2, Phys. Rev. Lett. **113**, 076802 (2014).

[21] M. Ugeda, A. Bradley, S.-F. Shi, F. Da Jornada, Y. Zhang, D. Qiu, S.-K. Mo, Z. Hussain, Z.-X. Shen, F. Wang, S. Louie, and M. Crommie, *Giant bandgap renormalization and excitonic effects in a monolayer transition metal dichalcogenide semiconductor*, Nat. Mater. **13**, 1091 (2014).

[22] P. Goli, J. Khan, D. Wickramaratne, R. K. Lake, and A. A. Balandin, *Charge density waves in exfoliated films of van der Waals materials: Evolution of Raman spectrum in* $TiSe_2$, Nano Lett. **12**, 5941 (2012).

[23] L. J. Li, W. J. Zhao, B. Liu, T. H. Ren, G. Eda, and K. P. Loh, *Enhancing charge-density-wave order in* 1*T*-$TiSe_2$ *nanosheet by encapsulation with hexagonal boron nitride*, Appl. Phys. Lett. **109**, 141902 (2016).

[24] P. Chen, Y.-H. Chan, M.-H. Wong, X.-Y. Fang, M. Y. Chou, S.-K. Mo, Z. Hussain, A.-V. Fedorov, and T.-C. Chiang, *Dimensional effects on the charge density waves in ultrathin films of* $TiSe_2$, Nano Lett. **16**, 6331 (2016).

[25] K. Sugawara, Y. Nakata, R. Shimizu, P. Han, T. Hitosugi, T. Sato, and T. Takahashi, *Unconventional charge-density-wave transition in monolayer* 1*T*-$TiSe_2$, ACS Nano **10**, 1341 (2016).

[26] M. D. Watson, A. Rajan, T. Antonelli, K. Underwood, I. Marković, F. Mazzola, O. J. Clark, G.-R. Siemann, D. Biswas, A. Hunter, S. Jandura, J. Reichstetter, M. McLaren, P. L. Fèvre, G. Vinai, and P. D. C. King, *Strong-coupling charge density wave in monolayer* $TiSe_2$, 2D Mater. **8**, 015004 (2020).

[27] T. Antonelli, A. Rajan, M. D. Watson, S. Soltani, J. Houghton, G.-R. Siemann, A. Zivanovic, C. Bigi, B. Edwards, and P. D. King, *Controlling the charge density wave transition in single-layer* $TiTe_{2x}$ $Se_{2(1-x)}$ *alloys by band gap engineering*, Nano Lett. **24**, 215 (2023).

[28] S. Kolekar, M. Bonilla, Y. Ma, H. Coy Diaz, and M. Batzill, *Layer- and substrate-dependent charge density wave criticality in* 1*T*-$TiSe_2$, 2D Mater. **5**, 015006 (2018).

[29] S. Kolekar, M. Bonilla, H. Coy Diaz, M. Hashimoto, D. Lu, and M. Batzill, *Controlling the charge density wave transition in monolayer* $TiSe_2$*: Substrate and doping effects*, Adv. Quantum Technol. **1**, 1800070 (2018).

[30] N. Ohba, K. Miwa, N. Nagasako, and A. Fukumoto, *First-principles study on structural, dielectric, and dynamical properties for three BN polytypes*, Phys. Rev. B **63**, 115207 (2001).

[31] A. Laturia, M. L. Van de Put, and W. G. Vandenberghe, *Dielectric properties of hexagonal boron nitride and transition metal dichalcogenides: From monolayer to bulk*, npj 2D Mater. Appl. **2**, 6 (2018).

[32] A. Pierret, D. Mele, H. Graef, J. Palomo, T. Taniguchi, K. Watanabe, Y. Li, B. Toury, C. Journet, P. Steyer, V. Garnier, A. Loiseau, J.-M. Berroir, E. Bocquillon, G. Fève, C. Voisin, E. Baudin, M. Rosticher, and B. Plaçais, *Dielectric permittivity, conductivity and breakdown field of hexagonal boron nitride*, Mater. Res. Express **9**, 065901 (2022).

[33] Y. Kang, D. Jeon, and T. Kim, *Local mapping of the thickness-dependent dielectric constant of* MoS_2, J. Phys. Chem. C **125**, 3611 (2021).

[34] L. J. Li, E. C. T. O'Farrell, K. P. Loh, G. Eda, B. Özyilmaz, and A. H. Castro Neto, *Controlling many-body states by the electric-field effect in a two-dimensional material*, Nature (London) **529**, 185 (2016).

[35] P. Chen, Y.-H. Chan, X.-Y. Fang, Y. Zhang, M. Y. Chou, S.-K. Mo, Z. Hussain, A.-V. Fedorov, and T.-C. Chiang, *Charge density wave transition in single-layer titanium diselenide*, Nat. Commun. **6**, 8943 (2015).

[36] A. Rajan, K. Underwood, F. Mazzola, and P. D. C. King, *Morphology control of epitaxial monolayer transition metal dichalcogenides*, Phys. Rev. Mater. **4**, 014003 (2020).

[37] B. Seredyński, R. Bożek, J. Suffczyński, J. Piwowar, J. Sadowski, and W. Pacuski, *Molecular beam epitaxy growth of* $MoTe_2$ *on hexagonal boron nitride*, J. Cryst. Growth **596**, 126806 (2022).

[38] D. Fu, X. Zhao, Y.-Y. Zhang, L. Li, H. Xu, A.-R. Jang, S. I. Yoon, P. Song, S. M. Poh, T. Ren, Z. Ding, W. Fu, T. J. Shin, H. S. Shin, S. T. Pantelides, W. Zhou, and K. P. Loh, *Molecular beam epitaxy of highly crystalline monolayer molybdenum disulfide on hexagonal boron nitride*, J. Am. Chem. Soc. **139**, 9392 (2017).

[39] W. Pacuski, M. Grzeszczyk, K. Nogajewski, A. Bogucki, K. Oreszczuk, J. Kucharek, K. E. Połczyńska, B. Seredyński, A. Rodek, R. Bożek, T. Taniguchi, K. Watanabe, S. Kret, J. Sadowski, T. Kazimierczuk, M. Potemski, and P. Kossacki, *Narrow excitonic lines and large-scale homogeneity of transition-metal dichalcogenide monolayers grown by molecular beam epitaxy on hexagonal boron nitride*, Nano Lett. **20**, 3058 (2020).

[40] H. Henck, D. Pierucci, G. Fugallo, J. Avila, G. Cassabois, Y. J. Dappe, M. G. Silly, C. Chen, B. Gil, M. Gatti, F. Sottile, F. Sirotti, M. C. Asensio, and A. Ouerghi, *Direct observation of the band structure in bulk hexagonal boron nitride*, Phys. Rev. B **95**, 085410 (2017).

[41] R. J. Koch, J. Katoch, S. Moser, D. Schwarz, R. K. Kawakami, A. Bostwick, E. Rotenberg, C. Jozwiak, and S. Ulstrup, *Electronic structure of exfoliated and epitaxial hexagonal boron nitride*, Phys. Rev. Mater. **2**, 074006 (2018).

[42] A. Rajan, S. Buchberger, B. Edwards, A. Zivanovic, N. Kushwaha, C. Bigi, Y. Nanao, B. K. Saika, O. R. Armitage, P. Wahl, P. Couture, and P. D. C. King, *Epitaxial growth of large-area monolayers and van der waals heterostructures of transition-metal chalcogenides via assisted nucleation*, Adv. Mater. **36**, 2402254 (2024).

[43] See Supplemental Material at http://link.aps.org/supplemental/10.1103/9trc-9865 for additional materials characterisation, ARPES data and fitting, and calculations of band renormalisation and nonlocal screening effects.

[44] I. C. Gerber and X. Marie, *Dependence of band structure and exciton properties of encapsulated* WSe_2 *monolayers on the hBn-layer thickness*, Phys. Rev. B **98**, 245126 (2018).

[45] K. F. Berggren and B. E. Sernelius, *Band-gap narrowing in heavily doped many-valley semiconductors*, Phys. Rev. B **24**, 1971 (1981).

[46] B. Bennett, R. Soref, and J. Del Alamo, *Carrier-induced change in refractive index of InP, GaAs and InGaAsP*, IEEE J. Quantum Electron. **26**, 113 (1990).

[47] A. Steinhoff, M. Rösner, F. Jahnke, T. O. Wehling, and C. Gies, *Influence of excited carriers on the optical and electronic properties of* MoS_2, Nano Lett. **14**, 3743 (2014).

[48] A. Chernikov, A. M. van der Zande, H. M. Hill, A. F. Rigosi, A. Velauthapillai, J. Hone, and T. F. Heinz, *Electrical tuning of exciton binding energies in monolayer* WS_2, Phys. Rev. Lett. **115**, 126802 (2015).

[49] S. Gao and L. Yang, *Renormalization of the quasiparticle band gap in doped two-dimensional materials from many-body calculations*, Phys. Rev. B **96**, 155410 (2017).

[50] D. Erben, A. Steinhoff, C. Gies, G. Schönhoff, T. O. Wehling, and F. Jahnke, *Excitation-induced transition to indirect band gaps in atomically thin transition-metal dichalcogenide semiconductors*, Phys. Rev. B **98**, 035434 (2018).

[51] Z. Qiu, M. Trushin, H. Fang, I. Verzhbitskiy, S. Gao, E. Laksono, M. Yang, P. Lyu, J. Li, J. Su, M. Telychko, K. Watanabe, T. Taniguchi, J. Wu, A. H. C. Neto, L. Yang, G. Eda, S. Adam, and J. Lu, *Giant gate-tunable bandgap renormalization and excitonic effects in a 2D semiconductor*, Sci. Adv. **5**, eaaw2347 (2019).

[52] C. Sahoo, Y. i. t. Veld, A. J. H. Jones, Z. Jiang, G. Lupi, P. E. Majchrzak, K. Hsieh, K. Watanabe, T. Taniguchi, P. Hofmann, J. A. Miwa, Y. P. Chen, M. Rösner, and S. Ulstrup, *Quasiparticle gap renormalization driven by internal and external screening in* WS_2 *device*, Phys. Rev. Lett. **135**, 056401 (2025).

[53] A. Schobert, J. Berges, E. G. C. P. Van Loon, M. A. Sentef, S. Brener, M. Rossi, and T. O. Wehling, *Ab initio electron-lattice downfolding: Potential energy landscapes, anharmonicity, and molecular dynamics in charge density wave materials*, SciPost Phys. **16**, 046 (2024).

[54] M. Rösner, C. Steinke, M. Lorke, C. Gies, F. Jahnke, and T. O. Wehling, *Two-dimensional heterojunctions from nonlocal manipulations of the interactions*, Nano Lett. **16**, 2322 (2016).

[55] A. Raja, A. Chaves, J. Yu, G. Arefe, H. M. Hill, A. F. Rigosi, T. C. Berkelbach, P. Nagler, C. Schüller, T. Korn, C. Nuckolls, J. Hone, L. E. Brus, T. F. Heinz, D. R. Reichman, and A. Chernikov, *Coulomb engineering of the bandgap and excitons in two-dimensional materials*, Nat. Commun. **8**, 15251 (2017).

[56] E. G. C. P. van Loon, M. Schüler, D. Springer, G. Sangiovanni, J. M. Tomczak, and T. O. Wehling, *Coulomb engineering of two-dimensional Mott materials*, npj 2D Mater. Appl. **7**, 47 (2023).

[57] C. Chen, X. Chen, W. Tang, Z. Li, S. Wang, S. Ding, Z. Kang, C. Jozwiak, A. Bostwick, E. Rotenberg, M. Hashimoto, D. Lu, J. P. C. Ruff, S. G. Louie, R. J. Birgeneau, Y. Chen, Y. Wang, and Y. He, *Role of electron-phonon coupling in excitonic insulator candidate* Ta_2NiSe_5, Phys. Rev. Res. **5**, 043089 (2023).

[58] K. F. Mak, K. He, C. Lee, G. H. Lee, J. Hone, T. F. Heinz, and J. Shan, *Tightly bound trions in monolayer* MoS_2, Nat. Mater. **12**, 207 (2013).

[59] A. Steinhoff, M. Florian, M. Rösner, G. Schönhoff, T. O. Wehling, and F. Jahnke, *Exciton fission in monolayer transition metal dichalcogenide semiconductors*, Nat. Commun. **8**, 1166 (2017).

[60] T. N. Lin, S. R. M. Santiago, S. P. Caigas, C. T. Yuan, T. Y. Lin, J. L. Shen, and Y. F. Chen, *Many-body effects in doped* WS_2 *monolayer quantum disks at room temperature*, npj 2D Mater. Appl. **3**, 46 (2019).

[61] Z. Torbatian and D. Novko, *Plasmon excitations across the charge-density-wave transition in single-layer* $TiSe_2$, J. Phys. Chem. Lett. **15**, 6045 (2024).

[62] J. Berges, N. Girotto, T. Wehling, N. Marzari, and S. Poncé, *Phonon self-energy corrections: To screen, or not to screen*, Phys. Rev. X **13**, 041009 (2023).

[63] E. G. C. P. van Loon, M. Rösner, M. I. Katsnelson, and T. O. Wehling, *Random phase approximation for gapped systems: Role of vertex corrections and applicability of the constrained random phase approximation*, Phys. Rev. B **104**, 045134 (2021).

[64] L. Waldecker, A. Raja, M. Rösner, C. Steinke, A. Bostwick, R. J. Koch, C. Jozwiak, T. Taniguchi, K. Watanabe, E. Rotenberg, T. O. Wehling, and T. F. Heinz, *Rigid band shifts in two-dimensional semiconductors through external dielectric screening*, Phys. Rev. Lett. **123**, 206403 (2019).

[65] Y. Lin, X. Ling, L. Yu, S. Huang, A. L. Hsu, Y.-H. Lee, J. Kong, M. S. Dresselhaus, and T. Palacios, *Dielectric screening of excitons and trions in single-layer* MoS_2, Nano Lett. **14**, 5569 (2014).

[66] S. Fragkos, H. Orio, N. G. Erhardt, A. Jabed, S. Sasi, Q. Courtade, M. Masilamani, M. Ünzelmann, F. Diekmann, B. Hildebrand *et al.*, *Electron-phonon-dominated charge-density-wave fluctuations in* $TiSe_2$ *accessed by ultrafast nonequilibrium dynamics*, arXiv:2507.12430.

[67] Y. Wakisaka, T. Sudayama, K. Takubo, T. Mizokawa, M. Arita, H. Namatame, M. Taniguchi, N. Katayama, M. Nohara, and H. Takagi, *Excitonic insulator state in* Ta_2NiSe_5 *probed by photoemission spectroscopy*, Phys. Rev. Lett. **103**, 026402 (2009).

[68] Y. F. Lu, H. Kono, T. I. Larkin, A. W. Rost, T. Takayama, A. V. Boris, B. Keimer, and H. Takagi, *Zero-gap*

semiconductor to excitonic insulator transition in Ta_2NiSe_5, Nat. Commun. **8**, 14408 (2017).

[69] Y. Jia *et al.*, *Evidence for a monolayer excitonic insulator*, Nat. Phys. **18**, 87 (2022).

[70] B. Sun, W. Zhao, T. Palomaki, Z. Fei, E. Runburg, P. Malinowski, X. Huang, J. Cenker, Y.-T. Cui, J.-H. Chu, X. Xu, S. S. Ataei, D. Varsano, M. Palummo, E. Molinari, M. Rontani, and D. H. Cobden, *Evidence for equilibrium exciton condensation in monolayer* WTe_2, Nat. Phys. **18**, 94 (2022).

[71] Y. Song, C. Jia, H. Xiong, B. Wang, Z. Jiang, K. Huang, J. Hwang, Z. Li, C. Hwang, Z. Liu, D. Shen, J. A. Sobota, P. Kirchmann, J. Xue, T. P. Devereaux, S.-K. Mo, Z.-X. Shen, and S. Tang, *Signatures of the exciton gas phase and its condensation in monolayer* 1*T*-$ZrTe_2$, Nat. Commun. **14**, 1116 (2023).

[72] Q. Gao, Y.-h. Chan, Y. Wang, H. Zhang, P. Jinxu, S. Cui, Y. Yang, Z. Liu, D. Shen, Z. Sun, J. Jiang, T. C. Chiang, and P. Chen, *Evidence of high-temperature exciton condensation in a two-dimensional semimetal*, Nat. Commun. **14**, 994 (2023).

[73] Q. Gao, Y.-h. Chan, P. Jiao, H. Chen, S. Yin, K. Tangprapha, Y. Yang, X. Li, Z. Liu, D. Shen, S. Jiang, and P. Chen, *Observation of possible excitonic charge density waves and metal–insulator transitions in atomically thin semimetals*, Nat. Phys. **20**, 597 (2024).

[74] J. Huang *et al.*, *Evidence for an excitonic insulator state in* $Ta_2Pd_3Te_5$, Phys. Rev. X **14**, 011046 (2024).

[75] S. Buchberger, Y. in 't Veld, A. Rajan, P. A. E. Murgatroyd, B. Edwards, B. K. Saika, N. Kushwaha, M. H. Visscher, J. Berges, D. Carbone, J. Osiecki, C. Polley, T. Wehling, and P. D. C. King, *Persistence of charge ordering instability to Coulomb engineering in the excitonic insulator candidate* $TiSe_2$ *(dataset)*, Dataset, University of St. Andrews Research Portal, 10.17630/45e7aa5c-c165-4869-8fca-35e7154f14f3 (2025).

[76] P. D. C. King, B. Edwards, S. Mo, T. Antonelli, E. A. Morales, L. Hart, and L. Trzaska, *Peaks: A* PYTHON *package for analysis of angle-resolved photoemission and related spectroscopies*, arXiv:2508.04803.

[77] M. Rösner, E. Şaşıoğlu, C. Friedrich, S. Blügel, and T. O. Wehling, *Wannier function approach to realistic Coulomb interactions in layered materials and heterostructures*, Phys. Rev. B **92**, 085102 (2015).

[78] L. Hedin, *New method for calculating the one-particle Green's function with application to the electron-gas problem*, Phys. Rev. **139**, A796 (1965).

[79] C. Steinke, T. O. Wehling, and M. Rösner, *Coulomb-engineered heterojunctions and dynamical screening in transition metal dichalcogenide monolayers*, Phys. Rev. B **102**, 115111 (2020).

[80] O. Parcollet, M. Ferrero, T. Ayral, H. Hafermann, I. Krivenko, L. Messio, and P. Seth, *TRIQS: A toolbox for research on interacting quantum systems*, Comput. Phys. Commun. **196**, 398 (2015).

[81] H. U. Strand, N. Wentzell, S. Kaeser, Y. in 't Veld, D. Simon, A. Hampel, M. Roesner, E. van Loon, O. Parcollet, O. Gingras, P. Dumitrescu, T. Hahn, and M. Zingl, TRIQS/tprf: Version 3.2.1 (2023), 10.5281/zenodo.13652322.

[82] G. Giuliani and G. Vignale, *Quantum Theory of the Electron Liquid* (Cambridge University Press, Cambridge, England, 2005).

[83] J. Comtet, A. Niguès, V. Kaiser, B. Coasne, L. Bocquet, and A. Siria, *Nanoscale capillary freezing of ionic liquids confined between metallic interfaces and the role of electronic screening*, Nat. Mater. **16**, 634 (2017).

[84] R. Akashi and R. Arita, *Development of density-functional theory for a plasmon-assisted superconducting state: Application to lithium under high pressures*, Phys. Rev. Lett. **111**, 057006 (2013).